

# Analytical Solution for Two-Phase Flow Within and Outside a Sphere under Pure Shear

S. Hier-Majumder<sup>†</sup>

Department of Earth Sciences, Royal Holloway University of London, Egham, TW20 0EX,  
Surrey, UK

(Received xx; revised xx; accepted xx)

This article presents a framework for building analytical solutions for coupled flow in two interacting multiphase domains. The coupled system consists of a multiphase sphere embedded in a multiphase substrate. Each of these domains consist of an interconnected, load-bearing, creeping matrix phase and an inviscid interstitial fluid phase. This article outlines techniques for building analytical solutions for velocity, pressure, and compaction within each domain, subject to boundary conditions of continuity of matrix velocity, normal traction, normal pressure gradient, and compaction at the interface between the two domains. The solutions, valid over a short period of time in the limit of small fluid fraction, are strongly dependent on the ratio of shear viscosities between the matrix phase in the sphere and the matrix phase in the substrate. Compaction and pressure drop across the interface, evaluated at the poles and the equator, are strongly dependent on the ratio of matrix shear viscosities in the two domains. When deformed under a pure shear deformation, the magnitude of flow within the sphere rapidly decreases with an increase in this ratio until it reaches a value of  $\sim 80$ , after which, the velocity within the sphere becomes relatively insensitive to the increase in the viscosity ratio.

## 1. Introduction

Coupled motion of two physically distinct phases dictates a number of natural phenomena such as the migration and storage of magma in the Earth's mantle, compaction of sedimentary basins, porous flow of hydrocarbon and ground water, and dynamics of melting of sea ice. Flow in such natural multiphase systems involves coupled conservation of mass, momentum, and energy between two distinct, coexisting phases. These conservation relations arise from flow in two interconnected phases: the load-bearing, creeping matrix and the inviscid interstitial fluid. A large body of publications studied the derivation of these coupled conservation equations, their stability, associated nonlinear phenomena, analytical, and numerical solutions, and their application to various natural phenomena (e.g. Barcilon & Lovera 1989; Bercovici *et al.* 2001*a,b*; Drew 1971, 1983; Hier-Majumder *et al.* 2006; McKenzie 1984; Ricard *et al.* 2001; Rudge 2014; Rudge *et al.* 2011; Simpson *et al.* 2010*a,b*; Spiegelman 1993*a,b*; Takei & Hier-Majumder 2009). Based on the results of these studies and natural observations, a few facts emerge about viscous multiphase flow in the nature. First, natural phenomena arising from multiphase flow can take place over a large variety of length scales. Second, many natural phenomena involve interaction between multiple domains consisting of multiphase aggregates. Such domains are often marked by contrasting effective physical properties and are separated by a distinct interface. Finally, during coupled flow of deforming multiphase aggregates,

<sup>†</sup> Email address for correspondence: saswata.hier-majumder@rhul.ac.uk

the weaker phase self segregates during the flow. Such self segregation of the weak phase is often the most interesting feature of natural multiphase flow as it has strong implications for storage, migrations, and stability of partial melt in the deep Earth or effective strength of the aggregate in the microscopic scale.

One important example of coupled multiphase flow comes from recent seismic observations at the Earth's core mantle boundary. The Earth's lower mantle, the bottom of the viscous, rocky layer above the metallic core, is marked by two large structures, located diametrically opposite to each other, one beneath Africa and the other beneath the Pacific ocean (McNamara *et al.* 2010). Often described as the Large Low Shear Velocity Provinces (LLSVPs), owing to their seismic signature, these structures are compositionally distinct from the rest of the mantle, contain multiple viscous solid phases of contrasting strength, and are marked by convective flows within their interior (Bower *et al.* 2011; McNamara *et al.* 2010). The bottom edges of the LLSVPs are marked by another set of patchy, smaller structures, called UltraLow Velocity Zones (ULVZs) (Rost *et al.* 2005; Rost & Revenaugh 2003; Williams & Garnero 1996). The location of ULVZs, also containing multiple solid and fluid phases, within the LLSVPs seem to suggest that the ULVZs are swept around and deformed by the flow within the LLSVPs (Bower *et al.* 2011; Hier-Majumder & Drombosky 2016; Hier-Majumder & Revenaugh 2010; McNamara *et al.* 2010). The ULVZs and LLSVPs are marked by sharp boundaries separating them from the surrounding mantle. To study the distribution of the weaker phases within the ULVZs, it is therefore crucial to understand the way the flow within these two multiphase domains with distinctive average physical properties are coupled (Hier-Majumder 2014; Hier-Majumder & Drombosky 2016; Hier-Majumder & Revenaugh 2010). In a recent study, Hier-Majumder & Drombosky (2016) outlined the nature of coupled flow within these two bodies. This study modeled the flow using boundary integral formulation of coupled Stokes flow within the ULVZ and the LLSVP. As a result, this study was unable to quantify the nature of compaction and segregation of the constituent phases.

A second example of coupled flow arises from observations on a different length scale. In the Earth's lower crust, viscous deformation of multiphase rocks can often be associated with characteristic structures in the microscopic scale. Deformation of these rocks, consisting of several different mineral phases, leads to the establishment of pockets of multiple weak mineral phases embedded in a substrate consisting of stronger mineral phases (Handy *et al.* 1999; Holyoke & Tullis 2006; Qi *et al.* 2013). As the deformation of these rocks facilitate the motion of overlying tectonic plates, the interaction between these pockets of weakness play an important role in establishing the effective strength of the rocks (Handy *et al.* 1999). Since both the substrate and the pockets consist of multiple phases, to understand the separation of phases within each of these domains the nature of coupling between the two flows are quite important.

Both of these natural examples demand a theoretical construct involving multiple, interacting domains of multiphase aggregates. Often one of these domains can be characterized by substantially different average physical properties, such as shear viscosity of the load-bearing matrix. In reconstructing geological events of past from microstructures, or to infer the nature of mantle flow from present day seismic observations in the Earth, it is crucial to understand the influence of such contrast in physical properties between different domains on the nature of flow and phase segregation within each domain.

Interaction between viscous bodies of single phase fluids, suspended in a single, viscous fluid phase, has been studied at length over the last several decades, building on the work of Taylor (1932). These studies investigated interaction between particles and substrates in areas including drop deformation (Li & Pozrikidis 1996; Manga & Stone

1995; Pozrikidis 1990), emulsions and foams (Li *et al.* 1995; Loewenberg & Hinch 1996), volcanology (Manga & Loewenberg 2001; Rust & Manga 2002), rheology (Li & Pozrikidis 1997; Manga *et al.* 1998; Taylor 1932), and microstructure in sintering materials (Hier-Majumder 2008, 2011; Hier-Majumder & Abbott 2010; Hopper 1993*a,b*; Kuiken 1993). The governing equations for these studies involve Stokes flow within two domains, the suspended drop and the medium of suspension. The mass and momentum conservation for Stokes flow is supplemented by a set of boundary conditions, typically continuity of velocity and balance of traction, often with a constant or spatially varying surface tension at the interface between the particle and the substrate (Pozrikidis 2001).

This work is motivated by the geological observations of multiphase-multidomain flows. While a substantial amount of work has been done in both areas of multidomain, single-phase flow and single-domain multiphase flow, the interaction between multiple multiphase domains remains relatively unexplored. This article presents analytical solutions for a spherical multiphase domain embedded in a multiphase substrate. This study focuses on understanding the dependence of velocity, fluid pressure, and compaction within and outside the sphere as a function of the ratio of matrix shear viscosities of the two domains. While previous studies of multidomain single-phase flow demonstrate that this ratio plays a crucial role in the velocity and pressure fields within each domain, the response of multidomain, multiphase flows to this ratio still remains unexplored. To describe the mass and momentum conservation within each domain, we follow the governing equations outlined by Bercovici *et al.* (2001*a,b*) and Ricard *et al.* (2001). Unlike the original work of Bercovici *et al.* where the primary variables are the velocity fields of the two phases, this work rewrites the momentum equation in terms of one velocity and one pressure (Alisic *et al.* 2014; Katz *et al.* 2007; Rhebergen *et al.* 2014, 2015; Rudge 2014).

The content of this article is divided into three major sections. We present derivation of the governing equations, boundary conditions, and nondimensionalization schemes in Section 2. In Section 3, we present the methods for building solution for velocity and pressure fields using vector harmonics and modified spherical Bessel functions. We also discuss general strategies for solution building for this class of problems in this section. Finally in Section 4 we present the results of coupled flow in the two domains. In this article, we primarily explore the role of the ratio of shear viscosity of the matrix phases within the sphere and the substrate. Finally, we present our conclusions in Section 5.

## 2. Theory

### 2.1. Governing equations

Consider a spherical, multiphase domain embedded in a multiphase substrate. Both of these domains consist of two interconnected phases: a load-bearing, viscous matrix and an inviscid interstitial fluid. We designate the sphere as the inner domain ( $\Omega_1$ ) and the substrate as the outer domain ( $\Omega_2$ ), separated by an interface  $\partial\Omega$ . The schematic diagram in Figure 1 outlines the domains, the boundaries, the key variables, and boundary conditions. We apply a known, external velocity to the substrate, which induces creeping motion of the matrix within both domains. Within each domain, flow of the matrix leads to matrix compaction and segregation of the interstitial fluid. Matrix flow, normal forces, flux of interstitial fluid, and compaction between the two domains, the sphere and the substrate, are controlled by a set of boundary conditions at the interface between the sphere and the substrate. We use primed variables for the substrate and unprimed variables for the sphere. During the derivation of the governing equations, however, we use unprimed variables, and notice that these generalized equations apply for both domains.

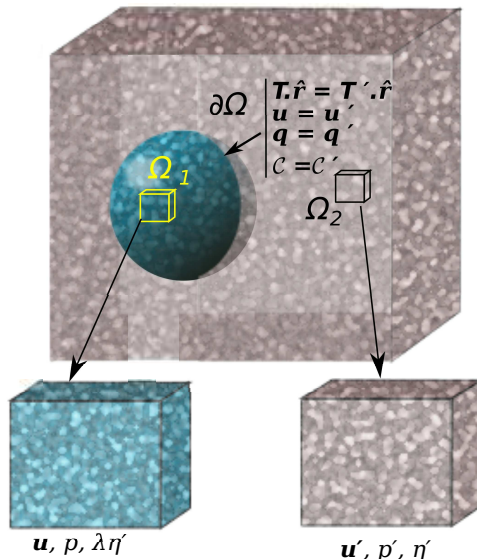


FIGURE 1. A schematic diagram showing the outline of the problem and the matching boundary condition at interface between the two domains. Both domains consist of a viscous matrix and an interstitial fluid. The ratio between the shear viscosity of the inner matrix over that of the outer matrix is given by  $\lambda$ . The two boundary conditions indicate continuity of velocity and traction across the interface. Two representative unit volumes within each domain are shown in zoom. Each of these unit volumes consist of a matrix and an interstitial fluid.

We use boldface serif font to denote vectors and boldface sans-serif fonts to denote tensors. Finally, we notice that the ratio of the shear viscosity of the matrix of the sphere and the matrix of the substrate is given by the dimensionless variable  $\lambda$ .

Within each domain, the volume fraction of the interstitial fluid is given by the variable  $\phi$ . While the density of all the phases are constant, compaction of the two-phase aggregate can lead to change in the total volume of the matrix and interstitial fluid in a unit volume. As a result, the aggregates in each domain are associated with an effective bulk viscosity (Bercovici *et al.* 2001a; McKenzie 1984; Ricard *et al.* 2001). Viscous flow of the interstitial fluid through an interconnected network of throats and pores is governed by Darcy flow (McKenzie 1984). Relative motion between the two phases leads to frictional resistance at the interface between the fluid and the matrix (Bercovici *et al.* 2001a; Hier-Majumder 2011). The constitutive equations for the effective physical properties, such as the bulk viscosity and frictional resistance arise from microstructural models implicitly assumed. While a detailed description of the microstructural models are beyond the scope of this article, the interested reader can find more detailed description in a number of published articles (Bercovici *et al.* 2001a; Drombosky & Hier-Majumder 2015; Hier-Majumder 2008; Hier-Majumder & Abbott 2010; Hier-Majumder & Drombosky 2015; King *et al.* 2011; Simpson *et al.* 2010a; Takei & Hier-Majumder 2009; Wimert & Hier-Majumder 2012).

The complete set of governing equations within each domain consists of a mass and momentum conservation equation for each phase supplemented by a set of constitutive equations arising from the conservation of entropy and Onsager principle. For the sake of brevity, the reader is referred to these references for a detailed derivation of the governing equations. Here we present a short derivation of the equations in terms of matrix velocity and reduced fluid pressure in appendix A.

In the absence of melting or freezing, the equation for conservation of mass of the

matrix can be expressed in terms of the material time derivative of the interstitial fluid volume fraction as

$$\frac{D\phi}{Dt} = \frac{\partial\phi}{\partial t} + \mathbf{u} \cdot \nabla\phi = (1 - \phi)\nabla \cdot \mathbf{u} \quad (2.1)$$

where  $\mathbf{u}$  is the velocity and  $1 - \phi$  is the volume fraction of the matrix. The material time derivative of the fluid volume fraction on the left hand side of equation (2.1) represents the rate of fluid loss or gain from a unit volume of the multiphase aggregate. The unit volumes within each domain are shown in the schematic diagram in Figure 1. Since the fluid volume fraction depends on time and space, this derivative is nonzero, rendering the matrix velocity divergent. Later in the solution building process, we define the divergence of the matrix velocity as compaction.

The mass conservation equation is supplemented by two coupled partial differential equations (PDEs) for momentum conservation as outlined in appendix A. Which leads to the following two PDEs in  $\mathbf{u}$  and the reduced pressure  $p$ , within each domain  $\Omega_i (i = 1, 2)$ ,

$$\nabla [\alpha_\phi \nabla \cdot \mathbf{u}] + \nabla \cdot [\eta_\phi \boldsymbol{\varepsilon}(\mathbf{u})] - \nabla p = 0 \quad (2.2)$$

$$\nabla \cdot [\mathbf{u} - \phi^2 \mathbf{M}_0 \cdot \nabla p] = 0, \quad (2.3)$$

where  $\mathbf{M}_0 = \mathbf{C}^{-1}$  is the mobility tensor (Hier-Majumder 2011). The mobility tensor is associated with the more commonly used permeability tensor in porous flow models. The functions  $\alpha_\phi$  and  $\eta_\phi$  are given by

$$\alpha_\phi = \frac{2\eta(1 - \phi)(2 - \phi)}{3\phi} = \beta\eta_\phi, \quad (2.4)$$

$$\eta_\phi = \eta(1 - \phi), \quad (2.5)$$

where  $\beta$  is a function of  $\phi$ . Similar to the formulations of Rhebergen *et al.* (2014, 2015) and Alisic *et al.* (2014),  $\alpha_\phi$  represents an effective bulk viscosity within each domain. Notice that this expression of  $\alpha_\phi$  becomes singular in the limit  $\phi \rightarrow 0$ . The effective bulk viscosity of a unit volume in a multiphase aggregate depends on certain assumptions about the distribution and geometry of the phases in the unit volume (Bercovici *et al.* 2001a; Simpson *et al.* 2010a). As  $\phi \rightarrow 0$ , these underlying assumptions become invalid and the effective bulk viscosity becomes unbounded. Despite the presence of this singularity, we notice that this term becomes large as the interstitial fluid volume fraction decreases, indicating that it requires more work to compact a relatively dry unit volume.

In both domains, the matrix acts as the load bearing unit (Bercovici *et al.* 2001a). As a result, the average normal traction across the sphere-substrate interface will be borne by the matrix on each domain. To evaluate this, we start with the definition of the stress tensor in the matrix,  $\mathbf{T}$ , using the constitutive relation,

$$\mathbf{T} = [\alpha \nabla \cdot \mathbf{u} - p] \mathbf{I} + \eta \boldsymbol{\varepsilon}(\mathbf{u}), \quad \text{in } \Omega_i (i = 1, 2) \quad (2.6)$$

where  $\alpha = \alpha_\phi / (1 - \phi)$ . For small values of  $\phi$ , ( $\phi \ll 1$ ),  $\eta = \eta_\phi$  and  $\alpha = \alpha_\phi$ . For the sake of simplicity, we build solutions in this limit through the rest of this manuscript and use the symbol  $\alpha$  to denote the effective bulk viscosity. We define the parameter  $\beta = \alpha / \eta$ , the ratio between the bulk and shear viscosities. We also assume that the role of gravity is negligible, such that the fluid pressure can be replaced by the reduced pressure.

## 2.2. Nondimensionalization

We nondimensionalize the lengths with a characteristic length scale  $L$ , and using a characteristic velocity of magnitude  $u_0$ , we nondimensionalize the velocity, stress, and pressure. Finally, we use a reference value of interstitial friction,  $c$  (Hier-Majumder

2011), to nondimensionalize the mobility. This leads to the following nondimensionalized variables marked by an asterisk (\*),

$$\mathbf{u} = u_0 \mathbf{u}^* \quad (2.7)$$

$$\mathbf{T}, p = \frac{\eta u_0}{L} (\mathbf{T}^*, p^*) \quad (2.8)$$

and

$$\mathbf{M}_0 = \frac{1}{c} \mathbf{M}^*. \quad (2.9)$$

Through the rest of the article, we drop the asterisk from the dimensionless variables, unless noted otherwise. In this notation, the nondimensional versions of the two momentum conservation equations (2.2) and (2.3) become,

$$\nabla [\alpha \nabla \cdot \mathbf{u}] + \nabla \cdot [\eta \varepsilon(\mathbf{u})] - \nabla p = 0 \quad (2.10)$$

$$\nabla \cdot \left[ \mathbf{u} - \left( \frac{\delta}{L} \right)^2 \mathbf{M} \cdot \nabla p \right] = 0, \quad (2.11)$$

where  $\delta = \sqrt{\eta/c}$  is called the compaction length of the matrix (Bercovici *et al.* 2001*a*; McKenzie 1984). It is a characteristic length scale over which pore fluid can significantly segregate from the matrix.

To build analytical solutions, we make a few more simplifying assumptions. First, we treat  $\alpha$  and  $\eta$  as constants. While both of these terms are dependent on  $\phi$  which can vary spatially and temporally, this assumption decouples such variations from our solutions (Rudge 2014). Spiegelman (1993*a,b*) also discuss the issues associated with this assumption. The analytical solutions presented here are valid only for very short periods of time following the onset of the flow, as the coupling between the terms discussed above become crucial for later stages of the flow. Next, we assume that the mobility of the fluid,  $c\mathbf{M}_0 = \mathbf{I}$ , rendering  $\mathbf{M}^* = \mathbf{I}$ . Finally, we assume that the compaction length,  $\delta$ , is equal to the characteristic length scale,  $L$ , of the matrix, and both are equal to the dimensional radius of the sphere. Rudge (2014) presents results for varying compaction length on the outer flow.

We can further simplify the the governing PDE (2.10) by noticing the identity,

$$\nabla \cdot \varepsilon(\mathbf{u}) = 2\nabla (\nabla \cdot \mathbf{u}) - \nabla \times \nabla \times \mathbf{u}. \quad (2.12)$$

Which, in addition to the assumptions discussed earlier, leads to the simplified PDEs in each domain  $\Omega_i (i = 1, 2)$ ,

$$\nabla (\nabla \cdot \mathbf{u}) - \frac{1}{\alpha + 2\eta} \nabla p - \frac{\eta}{\alpha + 2\eta} \nabla \times \nabla \times \mathbf{u} = 0. \quad (2.13)$$

$$\nabla \cdot \mathbf{u} - \nabla^2 p = 0. \quad (2.14)$$

We notice that these equations are similar in nature to Spiegelman (1993*a*). Next, we proceed to construct analytical solutions for the potential functions. Due to the linear nature of the governing equations, general solutions for the potentials, containing unknown constant coefficients, can be superposed to obtain general solutions for velocity and pressure. Values of these unknown coefficients are then obtained by matching the boundary conditions. I present the results for two types of problems based on two types of boundary conditions. These boundary conditions are discussed in section 2.3.

### 2.3. Boundary conditions and solution for the coefficients

This section presents solutions for the unknown constants in the formulation for velocity and pressure in the sphere and the surrounding substrate. The values of these unknown constants are determined from the boundary conditions. The boundary conditions themselves depend on the nature of the problem to be investigated. Here, two primary types of problems are identified. The first class of problems concerns the solutions internal only to the sphere. These group of solutions complement the solutions for the substrate only, as discussed by Rudge (2014). The second set of problems arise from coupling of the flow within the sphere and substrate. This set of problems are particularly interesting for studying the distribution of interstitial melt within the deformable sphere. While our approximation of constant  $\alpha$ ,  $\eta$ , and permeability restricts the validity of these solutions only during the onset of flow, they still provide useful insight into the nature of the flows.

For the first class of problems, the substrate is considered effectively rigid. As a result, the sphere remains undeformed during the flow. Under these conditions, the restrictions on the continuity of traction can be relaxed. A more interesting boundary condition for this problem is imposing a Neumann condition on pressure. As a general case, we can express these boundary conditions as

$$\left. \begin{aligned} \mathbf{u} &= \mathbf{u}_s, \\ \nabla p \cdot \hat{\mathbf{n}} &= q_s, \end{aligned} \right\} \text{ on } \partial\Omega \quad (2.15)$$

where  $\mathbf{u}_s$  is a prescribed matrix velocity at the surface and  $q_s$  is a prescribed interstitial fluid flux at the surface of the sphere. Inserting the definition of modified pressure from equation (A 9) into the Darcy equation, and nondimensionalizing, we obtain,

$$\Delta \mathbf{u} = \phi \nabla p. \quad (2.16)$$

The second boundary condition on the normal gradient of pressure, therefore, allows prescription of flux of the interstitial fluid in or out of the sphere. Such a prescription is desirable for problems involving an impermeable boundary or problems of passive (since no reaction is involved) interstitial fluid injection. Problems involving flooding of hydrocarbon reservoirs during secondary recovery fall in this category (Gunde *et al.* 2010). While this boundary condition prescribes the normal flow of interstitial fluid given by  $\Delta \mathbf{u} \cdot \hat{\mathbf{n}}$ , no restrictions are imposed on the tangential component of the segregation velocity. This component adjusts itself based on the solution for pressure.

The second class of problem constitutes coupling of flow between the sphere and the substrate, involving deformation of the boundary between the two domains. A number of previous studies on a similar problems for spherical, single-phase drops embedded in a single-phase substrate outline two criteria for the boundary condition (Hier-Majumder 2008, 2011; Hier-Majumder & Abbott 2010; Hopper 1993*a,b*; Kuiken 1993; Li & Pozrikidis 1996; Li *et al.* 1995; Loewenberg & Hinch 1996; Manga *et al.* 1998; Manga & Loewenberg 2001; Manga & Stone 1995; Pozrikidis 1990; Rust & Manga 2002; Taylor 1932).

The first criterion requires that the velocity within the two domains must be matched at the boundary. For example, if the surface of the sphere (the interface  $\partial\Omega$ ) is defined by a shape function  $F = 0$ , then, assuming that the matrix is the load-bearing phase, the kinetic equation governing the shape evolution of the sphere is given by (Eq. 11, Hier-Majumder 2008),

$$\frac{\partial F}{\partial t} + \mathbf{u} \cdot \hat{\mathbf{n}} = 0. \quad (2.17)$$

Thus, the surface is advected by the normal component of the matrix velocity. If the velocities on both sides of the interface are unmatched then the advection equation will lead to either protrusion of one domain into the other or creation of empty space between the two domains. For problems involving deformation of the interface, therefore, it is crucial to ensure the continuity of velocity across the interface.

In addition, the traction at the boundary between the sphere and the substrate must be matched in order to ensure that the sphere and the substrate exert equal and opposite forces on each other (Kim & Karilla 2005). This boundary condition is further resolved into two components, one normal to the interface, and the other tangential. In order to ensure equal and opposite forces, the normal component of the tractions from each domain must be equal. This is often named the Laplace boundary condition. The jump in the tangential component, arising from shear stresses has to be matched by the surface parallel gradient of surface tension force acting on the boundary. This component is called the Marangoni condition. In this analysis, we assume that there is no surface tension on  $\partial\Omega$ , thus Laplace and Marangoni terms associated with surface tension do not appear in this boundary condition (e.g. equation 5-70 in Leal 1992).

In addition to the continuity of velocity and normal traction, two other constraints arise from interstitial fluid flux and compaction. First, the solutions must ensure that the flux of interstitial fluid is matched across the interface between the two domains. As discussed above, this constraint can be imposed by matching the normal gradient of pressure across the boundary. Notice that this condition is not guaranteed by the continuity of velocity and traction. Finally, we require that compaction within both domains must be matched at the boundary also. As the results demonstrate, these constraints ensure a unique solution for the coupled multiphase, multidomain flow.

With these above constraints, we solve for the coefficients for the coupled flow problem subject to the boundary conditions,

$$\left. \begin{aligned} \mathbf{u} &= \mathbf{u}', \\ \mathbf{T} \cdot \hat{\mathbf{n}} &= \mathbf{T}' \cdot \hat{\mathbf{n}}, \\ \nabla p \cdot \hat{\mathbf{n}} &= \nabla p' \cdot \hat{\mathbf{n}}, \\ \mathcal{C} &= \mathcal{C}', \end{aligned} \right\} \text{ on } \partial\Omega \quad (2.18)$$

where compaction, given by the variable  $\mathcal{C}$ , is defined in the following section. In the following subsections, we present the solutions for the coefficients for the two types of problems discussed above.

### 3. Solution Building

#### 3.1. Potential functions

We seek to build analytical solutions for velocity and pressure within each domain using potential functions. For similar multidomain problems involving Stokes flow, typically vector harmonics are used to build vector and scalar potentials (Happel & Brenner 1983; Kim & Karilla 2005; Leal 1992). During two-phase flow, an additional potential is needed to account for the divergence of matrix velocity or compaction,  $\mathcal{C}$ , given by (Spiegelman 1993a)

$$\mathcal{C} = \nabla \cdot \mathbf{u}. \quad (3.1)$$

In a recent article, Rudge (2014) builds analytical solutions for flow in the substrate using Neuber-Papkovich potentials. In this method, one vector potential  $\boldsymbol{\varphi}$  and two scalar potentials,  $\mathcal{C}$  and  $\chi$ , are used to build the solutions. In order for the solutions to



be independent of coordinate system, these functions are built from the position vector  $\mathbf{r}$ . The matrix velocity and the reduced pressure within each domain can be expressed as a function of these potentials as,

$$\mathbf{u} = \nabla [\mathbf{r} \cdot \boldsymbol{\varphi} + \chi + \mathcal{C}] - 2\boldsymbol{\varphi} \quad (3.2)$$

$$p = 2\eta \nabla \cdot \boldsymbol{\varphi} + (\alpha + 2\eta) \mathcal{C}. \quad (3.3)$$

Substituting the potential forms of velocity and pressure from equations (3.2) and (3.3) into equations (2.13) and (2.14), we obtain three simpler PDEs,

$$\nabla^2 \boldsymbol{\varphi} = 0 \quad (3.4)$$

$$\nabla^2 \chi = 0 \quad (3.5)$$

$$\text{and} \quad (3.6)$$

$$\nabla^2 \mathcal{C} - \mathcal{C} = 0. \quad (3.7)$$

The definition of compaction,  $\mathcal{C}$  in equation (3.1) combined with the equation for mass conservation (2.1) yields

$$\frac{D\phi}{Dt} = (1 - \phi)\mathcal{C}. \quad (3.8)$$

For very small fluid fractions,  $\phi \ll 1$  and  $D\phi/Dt \approx \mathcal{C}$ . Which implies, in the early stages of compaction containing a small volume fraction of pore fluid, the fluid will accumulate ( $D\phi/Dt > 0$ ) in regions of positive compaction (dilation) and drain out of regions of negative compaction. While this is a zeroth order approximation, this relation provides us with an insight about the nature of phase segregation within each domain as a result of the coupled flow.

A general far-field flow in the substrate can consist of a straining component, a rotating component, and a translating component (Leal 1992, Ch. 4). For solutions arising from a purely straining flow, the rotating and translating components of the far-field flow can be neglected. As we focus on the flow field due to a purely straining flow, we will use this strategy for building the solution. The straining component is built from the symmetric strain rate tensor  $\dot{\mathbf{E}}$ , such that  $Tr(\dot{\mathbf{E}}) = 0$ . The primary variables, velocity and pressure, are built from the characteristic scalar  $\dot{\mathbf{E}} : \mathbf{r}\mathbf{r}$ , and two characteristic vectors,  $\dot{\mathbf{E}} \cdot \mathbf{r}$  and  $(\dot{\mathbf{E}} : \mathbf{r}\mathbf{r}) \mathbf{r}$ , respectively.

While the influence of far field flow is incorporated in the solution by the methods discussed above, the remaining part of the solution is built from fundamental solutions to the Laplace and the modified Helmholtz equations. An important consideration in building solutions is the behavior of the solution at the origin  $r = 0$  and at large distances away from the sphere,  $r \rightarrow \infty$ . We discuss these issues in the next subsection.

At this stage, it is useful to define a few additional relations for derived variables in terms of these potential functions.

$$\dot{\mathbf{e}} = \frac{1}{2} \varepsilon(\mathbf{u}) = (\nabla \nabla \boldsymbol{\varphi}) \cdot \mathbf{r} + \nabla \nabla (\chi + \mathcal{C}) \quad (3.9)$$

$$P_m = 2\eta \nabla \cdot \boldsymbol{\varphi} + (\alpha + \bar{\eta}) \mathcal{C} \quad (3.10)$$

$$\mathbf{T} = 2\eta \left[ -(\nabla \cdot \boldsymbol{\varphi} + \mathcal{C}) + \frac{1}{2} \varepsilon(\mathbf{u}) \right] \quad (3.11)$$

$$\mathbf{t} = \mathbf{T} \cdot \hat{\mathbf{n}} = \frac{2\eta}{r} \left[ -(\nabla \cdot \boldsymbol{\varphi}) \mathbf{r} - \mathcal{C} \mathbf{r} + \frac{1}{2} \varepsilon(\mathbf{u}) \cdot \mathbf{r} \right], \quad (3.12)$$

where  $\bar{\eta} = 2\eta(3\phi - 2)/(3\phi)$ .

In the following subsections, we discuss the selection of functions involved in the solution building.

### 3.2. Growing and decaying functions

We build solutions for the potential functions  $\varphi$  and  $\chi$  from vector harmonic functions (Leal 1992). Vector harmonics are derived from the fundamental solution to the Laplace equation, which satisfies the inhomogeneous equation,

$$-\nabla^2 \chi = \delta^{(3)}(\mathbf{r}), \quad (3.13)$$

where  $\delta^{(3)}(\mathbf{r})$  is the three dimensional Dirac delta function centered around a point located at position  $\mathbf{r}$ . One family of solutions, decaying harmonics, are built from the fundamental solution and its successive derivatives Leal (1992)[Ch. 4].

While the vector harmonic functions are useful for building solutions for the vector and scalar Laplace equations, the presence of the modified Helmholtz equation calls for an additional fundamental solution. We notice that the fundamental solution to the modified Helmholtz equation should satisfy the equation,

$$-\mathcal{C} + \nabla^2 \mathcal{C} = \delta^{(3)}(\mathbf{r}). \quad (3.14)$$

Following a similar reason as above, the solutions to the modified Helmholtz equation arising from the internal and the external flow can be built from the fundamental solution and its derivatives decaying as  $r \rightarrow 0$  and  $r \rightarrow \infty$ , respectively. For the internal flow, we build solutions based on the modified spherical Bessel functions of the first kind (Arfken & Weber 1995, pp. 689).

The modified Bessel functions of the first kind decay with  $r$  and are bound to finite values as  $r \rightarrow 0$ . A useful recurrence relation involving these functions is

$$\nabla \left( \frac{i_n(r)}{r^n} \right) = \frac{i_{n+1}(r)}{r^{n+1}} \mathbf{r}. \quad (3.15)$$

As discussed by Rudge (2014), the solution for compaction in the substrate can be built from the modified spherical Bessel functions of the second kind. Another useful identity involving these functions is

$$\nabla \left( \frac{k_n(r)}{r^n} \right) = -\frac{k_{n+1}(r)}{r^n} \mathbf{r}. \quad (3.16)$$

### 3.3. Solutions for internal flow

In this article, we set the origin at the center of the sphere. Consequently, the solutions for the interior of the sphere need to be built from growing harmonics, preventing singular solutions at the origin. As  $r$  is always bound by a finite value, the solution is guaranteed to be bound by finite values on both ends. Since the potential functions contain one vector and two scalar potentials, we build the solution by combining lower order growing vector harmonic functions and the spherical Bessel functions of the first kind with the characteristic scalar  $\hat{\mathbf{E}}: \mathbf{r}\mathbf{r}$ , and two characteristic vectors  $\hat{\mathbf{E}} \cdot \mathbf{r}$  and  $(\hat{\mathbf{E}}: \mathbf{r}\mathbf{r})\mathbf{r}$ .

The resulting solutions call for the introduction of 3 unknown coefficients,  $F$ ,  $G$ , and

$H$ , leading to the following definitions of the potential functions

$$\varphi = \frac{2F}{5} (1 - r^2) \dot{\mathbf{E}} \cdot \mathbf{r} + \mathbf{r} \left( \dot{\mathbf{E}} : \mathbf{r}\mathbf{r} \right) \quad (3.17)$$

$$\chi = G \left( \dot{\mathbf{E}} : \mathbf{r}\mathbf{r} \right) \quad (3.18)$$

$$\mathcal{C} = \frac{H}{r^2} i_2(r) \left( \dot{\mathbf{E}} : \mathbf{r}\mathbf{r} \right). \quad (3.19)$$

Using these definitions, the expressions for velocity, reduced pressure, normal traction, and the normal component of pressure gradient are given by,

$$\mathbf{u} = 2 \left[ Fr^2 + G + H \frac{i_2(r)}{r} \right] \dot{\mathbf{E}} \cdot \mathbf{r} + \left[ H \frac{i_3(r)}{r^3} - \frac{4F}{5} \right] \left( \dot{\mathbf{E}} : \mathbf{r}\mathbf{r} \right) \mathbf{r}, \quad (3.20)$$

$$p = \left[ \frac{42F\eta}{5} + H(\alpha + 2\eta) \frac{i_2(r)}{r^2} \right] \left( \dot{\mathbf{E}} : \mathbf{r}\mathbf{r} \right), \quad (3.21)$$

$$\begin{aligned} \mathbf{T} \cdot \mathbf{r} = & 2\eta \left[ -\frac{19}{5} - \frac{4Hi_3(r)}{r^3} \right] \left( \dot{\mathbf{E}} : \mathbf{r}\mathbf{r} \right) \mathbf{r} \\ & + 2\eta \left[ \frac{16r^2}{5} + 2G + 2H \left( \frac{i_3(r)}{r} + \frac{i_2(r)}{r^2} \right) \right] \dot{\mathbf{E}} \cdot \mathbf{r}, \end{aligned} \quad (3.22)$$

$$\nabla p \cdot \mathbf{r} = \left[ \frac{84F\eta}{5} + H(\alpha + 2\eta) \left( \frac{2i_2(r)}{r^2} + \frac{i_3(r)}{r} \right) \right] \left( \dot{\mathbf{E}} : \mathbf{r}\mathbf{r} \right). \quad (3.23)$$

In addition to these variables, we are also interested in calculating the tensor  $\dot{\mathbf{e}}$ . We find that an additional quantity,  $\mathcal{E}$ , is introduced,

$$\begin{aligned} \dot{\mathbf{e}} = & \left[ \frac{6F}{5} + 2H \frac{i_3(r)}{r^3} \right] \mathcal{E} + \left[ 2Fr^2 + 2G + 2H \frac{i_2(r)}{r^2} \right] \dot{\mathbf{E}} \\ & + \left[ -\frac{4F}{5} + H \frac{i_3(r)}{r^3} \right] \left( \dot{\mathbf{E}} : \mathbf{r}\mathbf{r} \right) \mathbf{I} + \left[ H \frac{i_4(r)}{r^4} \right] \left( \dot{\mathbf{E}} : \mathbf{r}\mathbf{r} \right) \mathbf{r}\mathbf{r} \end{aligned} \quad (3.24)$$

$$(3.25)$$

where the symmetric dyadic product  $\mathcal{E}$  is given by,

$$\mathcal{E} = \mathbf{r} \left( \dot{\mathbf{E}} \cdot \mathbf{r} \right) + \left( \dot{\mathbf{E}} \cdot \mathbf{r} \right) \mathbf{r}. \quad (3.26)$$

Next, we plan to build solutions for external flow, using similar functions of the far-field straining flow but with decaying functions of  $r$ .

### 3.4. Solutions for external flow

In building solutions for the external flow, we recognize that the solution should consist of two parts. One part, which we can call a perturbation flow, arises from the interaction between the substrate and the sphere through the boundary conditions imposed at their interface. This perturbing flow should decay away from the sphere. Thus, we express the total velocity,  $\mathbf{u}'$ , as a sum of a far-field uniform straining flow  $\mathbf{u}^\infty$  and the local, perturbing flow

$$\mathbf{u}' = \nabla [\mathbf{r} \cdot \boldsymbol{\varphi}' + \chi' + \mathcal{C}'] - 2\boldsymbol{\varphi}' + \mathbf{u}^\infty, \quad (3.27)$$

subject to the constraint that as  $r \rightarrow \infty$ ,  $\mathbf{u}' \rightarrow \mathbf{u}^\infty$ . Next, we want to prescribe a form for  $\mathbf{u}^\infty$ , in terms of a characteristic vector associated with the straining flow. One obvious choice is the simplest vector  $\dot{\mathbf{E}} \cdot \mathbf{r}$ , leading to  $\mathbf{u}^\infty = \dot{\mathbf{E}} \cdot \mathbf{r}$  (Ch. 4 Leal 1992). Notice that

since  $Tr(\dot{\mathbf{E}}) = 0$ ,  $\nabla \cdot \mathbf{u}^\infty = 0$ . Consequently, the far-field strain doesn't introduce any additional terms associated with compaction.

It is worth noting that for a more general solution, the external flow can be expressed as a sum of a straining flow, a translating flow, and a rotating flow. We ignore the two latter components. Consequently, our results apply for irrotational straining flow only. In specific, we focus on flow arising from pure shear. To build solutions for a simple shear straining flow, the rotational component need to be included while building the vector  $\mathbf{u}^\infty$  (See Ch. 4 of Leal 1992, for more discussions).

Similar to the solutions for internal flow, we build the vector and scalar potential functions from the characteristic vector  $\dot{\mathbf{E}} \cdot \mathbf{r}$  and the scalar  $\dot{\mathbf{E}} : \mathbf{r}\mathbf{r}$ , leading to the introduction of three new unknown constants,  $M, N$ , and  $L$ , whose value will be determined during the next stage.

$$\varphi' = -\frac{L}{r^3} \dot{\mathbf{E}} \cdot \mathbf{r}, \quad (3.28)$$

$$\chi' = \frac{3M}{r^5} (\dot{\mathbf{E}} : \mathbf{r}\mathbf{r}), \quad (3.29)$$

$$C' = N \frac{k_2(r)}{r^2} (\dot{\mathbf{E}} : \mathbf{r}\mathbf{r}). \quad (3.30)$$

Since all three of these functions are associated with the coupled flow, they all decay further away from the sphere.

Employing the definitions of the velocity and stresses as above, and utilizing the recurrence relations of the modified spherical Bessel functions, the solutions for velocity, pressure, and traction are given by,

$$\mathbf{u}' = \left[ \frac{6M}{r^5} + 2N \frac{k_2(r)}{r^2} + 1 \right] \dot{\mathbf{E}} \cdot \mathbf{r} + \left[ \frac{3L}{r^5} - \frac{15M}{r^7} - N \frac{k_3(r)}{r^3} \right] (\dot{\mathbf{E}} : \mathbf{r}\mathbf{r}) \mathbf{r} \quad (3.31)$$

$$p' = \left[ \frac{6L\eta'}{r^5} + (\alpha' + 2\eta') \frac{Nk_2(r)}{r^2} \right] (\dot{\mathbf{E}} : \mathbf{r}\mathbf{r}) \quad (3.32)$$

$$\begin{aligned} \mathbf{T}' \cdot \mathbf{r} = & 2\eta' \left[ -\frac{12L}{r^5} + \frac{60M}{r^7} + \frac{4Nk_3(r)}{r^3} \right] (\dot{\mathbf{E}} : \mathbf{r}\mathbf{r}) \mathbf{r} \\ & + 2\eta' \left[ \frac{3L}{r^3} - \frac{24M}{r^5} + 2N \left( \frac{k_2(r)}{r^2} - \frac{k_3(r)}{r} \right) + 1 \right] \dot{\mathbf{E}} \cdot \mathbf{r}, \end{aligned} \quad (3.33)$$

$$\nabla p' \cdot \mathbf{r} = \left[ -\frac{18L\eta'}{r^5} + N(\alpha' + 2\eta') \left( \frac{2k_2(r)}{r^2} - \frac{k_3(r)}{r} \right) \right] (\dot{\mathbf{E}} : \mathbf{r}\mathbf{r}). \quad (3.34)$$

Similar to the internal flow, we see the introduction of the additional symmetric dyad  $\mathcal{E}$  in the definition of the strain rate field  $\dot{\mathbf{e}}$ ,

$$\begin{aligned} \dot{\mathbf{e}} = & \left[ -\frac{15L}{r^7} + \frac{105M}{r^9} + \frac{Nk_4(r)}{r^4} \right] (\dot{\mathbf{E}} : \mathbf{r}\mathbf{r}) \mathbf{r}\mathbf{r} \\ & + \left[ \frac{3L}{r^5} - \frac{30M}{r^7} - \frac{2Nk_3(r)}{r^3} \right] \mathcal{E} + \left[ \frac{3L}{r^5} - \frac{15M}{r^7} - \frac{Nk_3(r)}{r^3} \right] (\dot{\mathbf{E}} : \mathbf{r}\mathbf{r}) \mathbf{I} \\ & + \left[ \frac{6M}{r^5} + \frac{2Nk_2(r)}{r^2} + 1 \right] \dot{\mathbf{E}}. \end{aligned} \quad (3.35)$$

Similar to the definitions of the velocity and traction vectors for the internal flow, the variables for the external flow are composed of two characteristic vectors,  $\dot{\mathbf{E}} \cdot \mathbf{r}$  and  $(\dot{\mathbf{E}} : \mathbf{r}\mathbf{r}) \mathbf{r}$ . The next step in the solution building involves matching the coefficients of these vectors at the interface using the boundary conditions given in equation (2.18).

Finally, we define the strain rate tensor  $\dot{\mathbf{E}}$  as

$$\dot{\mathbf{E}} = \begin{bmatrix} \frac{1}{2} & 0 & 0 \\ 0 & \frac{1}{2} & 0 \\ 0 & 0 & -1 \end{bmatrix}. \quad (3.36)$$

### 3.5. Coefficients for internal flow

#### 3.5.1. Straining flow

Consider an impermeable sphere subjected to a straining flow. Since the segregation velocity of the interstitial fluid from the matrix is governed by the normal component of the pressure gradient, we can rewrite the boundary conditions in equation (2.15) as,

$$\left. \begin{aligned} \mathbf{u} &= \dot{\mathbf{E}} \cdot \mathbf{r}, \\ \nabla p \cdot \hat{\mathbf{n}} &= 0, \end{aligned} \right\} \text{ on } \partial\Omega \quad (3.37)$$

Using the coefficients of the terms in equations (3.20) and equation (3.23), we arrive at the following three algebraic equations,

$$1 = 2Fa^2 + 2G + 2\frac{Hi_2(a)}{a^2}, \quad (3.38)$$

$$0 = \frac{Hi_3(a)}{a^3} - \frac{4F}{5}, \quad (3.39)$$

$$0 = \frac{84F\eta}{5} + H(\alpha + 2\eta) \left( \frac{2i_2(a)}{a^2} + \frac{i_3(a)}{a} \right). \quad (3.40)$$

Solution of these equations leads to

$$F = 0, \quad (3.41)$$

$$G = \frac{1}{2}, \quad (3.42)$$

$$H = 0. \quad (3.43)$$

As a result, the internal velocity mimics the straining flow.

#### 3.5.2. Passive melt injection

A second interesting case involves melt injection into the sphere. To prescribe a spatially varying melt injection leading to a nontrivial solution within the sphere, we chose the following

$$\left. \begin{aligned} \mathbf{u} &= 0, \\ \nabla p \cdot \hat{\mathbf{n}} &= \dot{\mathbf{E}} : \mathbf{r}\mathbf{r}. \end{aligned} \right\} \text{ on } \partial\Omega \quad (3.44)$$

Substituting the solutions for pressure and velocity in these boundary conditions, we arrive at the following three algebraic equations

$$0 = 2Fa^2 + 2G + 2\frac{Hi_2(a)}{a^2}, \quad (3.45)$$

$$0 = \frac{Hi_3(a)}{a^3} - \frac{4F}{5}, \quad (3.46)$$

$$1 = \frac{84F\eta}{5} + H(\alpha + 2\eta) \left( \frac{2i_2(a)}{a^2} + \frac{i_3(a)}{a} \right). \quad (3.47)$$

Solution to these equations lead to the three following values for coefficients,  $F, G$ , and

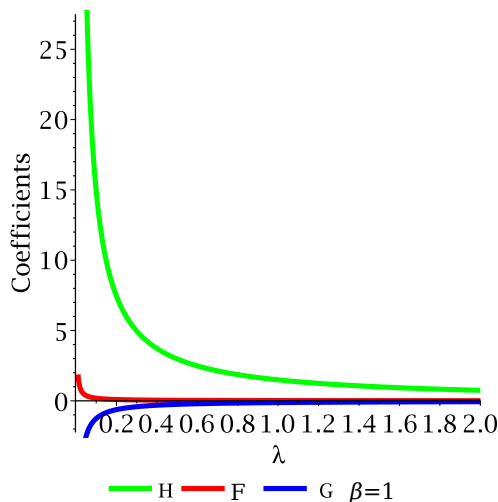


FIGURE 2. A plot of the coefficients  $F$ ,  $G$ , and  $H$  for internal flow as a function of  $\eta$ , during the passive melt injection problem. In this plot, we set  $a = 1$  and  $\beta = \alpha/\eta = 1$ .

$H$ ,

$$F = \frac{5}{4} \frac{i_3(a)}{(a^2 i_3(a) + 2a i_2(a)) \alpha + ((2a^2 + 21) i_3(a) + 4a i_2(a)) \eta} \quad (3.48)$$

$$G = -\frac{1}{4} \frac{a (5a i_3(a) + 4 i_2(a))}{(a^2 i_3(a) + 2a i_2(a)) \alpha + ((2a^2 + 21) i_3(a) + 4a i_2(a)) \eta} \quad (3.49)$$

$$H = \frac{5}{4} \frac{i_3(a)}{(a^2 i_3(a) + 2a i_2(a)) \alpha + ((2a^2 + 21) i_3(a) + 4a i_2(a)) \eta}. \quad (3.50)$$

The plots in Figure 2 depict the variation in these coefficients, as a function of the matrix viscosity  $\eta$ , for a value of  $\beta = \alpha/\eta = 1$  and  $a = 1$ . As the plot indicates, the magnitude of the coefficients decrease, indicating a general reduction in the magnitude of the flow as the matrix becomes more viscous.

### 3.6. Coefficients for coupled flow

We next proceed to match the boundary conditions in equation (2.18). The solutions contain six unknown constants,  $F, G, H, M, N$  and  $L$ . To solve for these constants, we match the coefficients of the characteristic vectors arising from the far-field flow in the expression for tractions and velocities at the interface between the sphere and the substrate in equation (2.18), leading to the following four equations

$$0 = 2Fa^2 + 2G + 2\frac{Hi_2(a)}{a^2} - 6\frac{M}{a^5} - 2\frac{Nk_2(a)}{a^2} - 1 \quad (3.51)$$

$$0 = \frac{Hi_3(a)}{a^3} - 4/5F - 3\frac{L}{a^5} + 15\frac{M}{a^7} + \frac{Nk_3(a)}{a^3} \quad (3.52)$$

$$0 = \lambda \left( -\frac{19F}{5} - 4\frac{Hi_3(a)}{a^3} \right) + 12\frac{L}{a^5} - 60\frac{M}{a^7} - 4\frac{Nk_3(a)}{a^3} \quad (3.53)$$

$$0 = \lambda \left( \frac{16Fa^2}{5} + 2G + 2H \left( \frac{i_3(a)}{a} + \frac{i_2(a)}{a^2} \right) \right) - 3\frac{L}{a^3} + 24\frac{M}{a^5} - 2N \left( \frac{k_2(a)}{a^2} - \frac{k_3(a)}{a} \right) - 1 \quad (3.54)$$

where  $\lambda = \eta/\eta'$ . Notice that since  $r = a$  on  $\partial\Omega$ , the equations derived from the boundary conditions are independent of  $r$ . Also, as the terms in the equations above are coefficients of the characteristic vector and scalars derived from  $\dot{\mathbf{E}}$  in equations, (3.20),(3.31),(3.23), and (3.33), they are also independent of  $\dot{\mathbf{E}}$ .

In order to uniquely determine all 6 coefficients, we need two additional equations. Continuity of interstitial fluid flux across the interface between the sphere and the substrate requires that the normal component of pressure gradient is continuous across the interface. Substituting the solutions into equations (3.23) and (3.34), we obtain the fifth equation,

$$\lambda \left[ \frac{84}{5} F + (\beta + 2) H \left( \frac{2i_2(a)}{a^2} + \frac{i_3(a)}{a} \right) \right] = -\frac{18}{a^5} L + (\beta + 2) N \left( -\frac{k_3(a)}{a} + \frac{2k_2(a)}{a^2} \right) \quad (3.55)$$

The final equation can be derived by setting compaction within and outside the sphere at  $r = a$  in equations (3.19) and (3.30),

$$\frac{i_2(a)}{a^2} H = \frac{k_2(a)}{a^2} N. \quad (3.56)$$

The above six equations allow a unique solution for all six constants involved in the potential functions. Solving these equations, and setting  $a = 1$ , we get the following values for the constants as functions of  $\lambda$  and  $\beta = \alpha/\eta$ ,

$$F = -15.55 \frac{(\lambda - 1)^2}{f(\lambda, \beta)}$$

$$G = -\frac{2.5 (7.50 \beta - 31.69) \lambda^2 - 2.5 (17.82 \beta + 40.71) \lambda}{f(\lambda, \beta)} \quad (3.57)$$

$$- \frac{24.22 \beta + 152.45}{f(\lambda, \beta)} \quad (3.58)$$

$$H = \frac{1468.0 (\lambda + 0.8421) (\lambda - 1.0)}{f(\lambda, \beta)} \quad (3.59)$$

$$L = -\frac{(12.49 \beta + 10.47) \lambda^3 + (17.20 \beta + 63.45) \lambda^2}{f(\lambda, \beta)} + \frac{(13.55 \beta + 41.63) \lambda + 16.15 \beta + 32.31}{f(\lambda, \beta)} \quad (3.60)$$

$$M = -\frac{(2.09 + 2.50 \beta) \lambda^3 + (51.50 + 3.44 \beta) \lambda^2}{f(\lambda, \beta)} + \frac{(15.98 + 2.71 \beta) \lambda + 37.63 + 3.23 \beta}{f(\lambda, \beta)} \quad (3.61)$$

$$N = \frac{40.79 (\lambda + 0.8421) (\lambda - 1.0)}{f(\lambda, \beta)} \quad (3.62)$$

where  $f(\lambda, \beta)$  is a polynomial of  $\lambda$  given by

$$f(\lambda, \beta) = (14.99 \beta + 12.56) \lambda^3 + (58.12 \beta + 119.5) \lambda^2 + (72.83 \beta + 169.9) \lambda + 29.06 \beta + 48.02. \quad (3.63)$$

Unlike solutions for coupled flow in single phase domains and uncoupled flow in a multiphase domain, the coefficients shown above are functions of both  $\lambda$  and  $\beta$ . This demonstrates the importance of the ratio of matrix shear viscosities in coupled multidomain, multiphase flow. Previous studies in magma dynamics, owing to the consideration

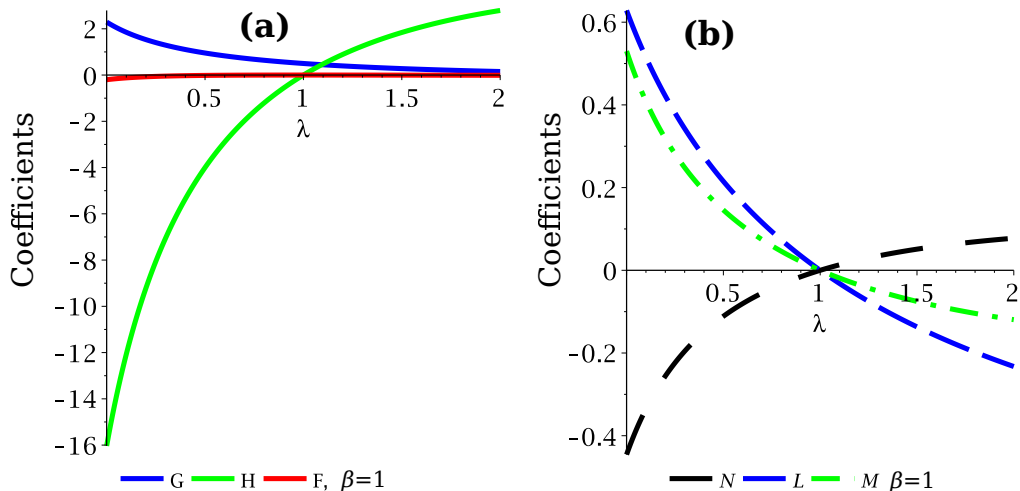


FIGURE 3. Plot of the coefficients for (a) internal and (b) external flow, as function of  $\lambda$ , the ratio of shear viscosities of the matrices in the sphere and the substrate. In these plots,  $a = 1$  and  $\beta = 1$ .

of a single domain, were unable to address this phenomenon. As the results in the following section demonstrate, the nature of matrix compaction and segregation of the interstitial fluid phase, at least in the limit of small time assumption, is reversed when the matrix within the sphere has a lower shear viscosity than the matrix of the substrate.

The plots in Figure 3 illustrate the dependence of the coefficients on  $\lambda$ . The coefficients for the internal flow are plotted in panel (a), while panel (b) describes the coefficients for the outer flow. In both series of plots,  $\alpha = \eta(\beta = 1)$  and  $a = 1$ . An important change in the coupled flow takes place at  $\lambda = 1$ . All three coefficients for the outer flow become zero at  $\lambda = 1$ , indicating that the external flow is described by the imposed infinite flow  $\mathbf{u}^\infty = \dot{\mathbf{E}} \cdot \mathbf{r}$ . Such a behavior in the coupled flow is expected as the perturbation to the infinite flow is caused by the contrast in the matrix viscosities in the two domains. In the absence of viscosity contrast, the perturbation is removed and flow within both domains is governed by the infinite flow. This situation is similar to previous studies of zeroth order two-phase flow, in the limit of small time and constant interstitial fluid volume fraction,  $\phi$ .

## 4. The influence of viscosity ratios on coupled flow

### 4.1. Field variables within both domains

The value of  $\lambda$  exerts a significant influence on the magnitude of velocity within the sphere. The velocity vectors both within and outside the sphere are displayed in Figure 4. The color and length of the vector arrows are proportional to the magnitude of the vectors. For all three visualizations,  $\beta = 1$ . The most remarkable feature is the rapid reduction in the magnitude of the internal flow as the value of  $\lambda$  increases from 0 to 10. This behavior is principally guided by the influence of  $\lambda$  on the coefficients as discussed above. With an increase in the internal viscosity, the magnitude of the flow in the interior of the sphere diminishes. For the value of  $\lambda = 1$ , the velocity within and outside the sphere are continuous and are equal to  $\mathbf{u}^\infty$ .



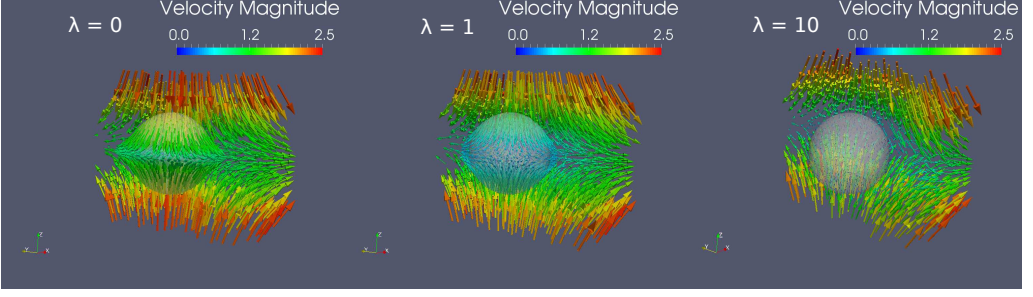


FIGURE 4. Velocity field within and outside the sphere for 3 different values of  $\lambda$ . In these visualizations with an imposed pure shear flow, the values of  $\beta$  and  $a$  are both unity. The color and length of the vector arrows scale with the magnitude of velocity as shown in the colorbar.

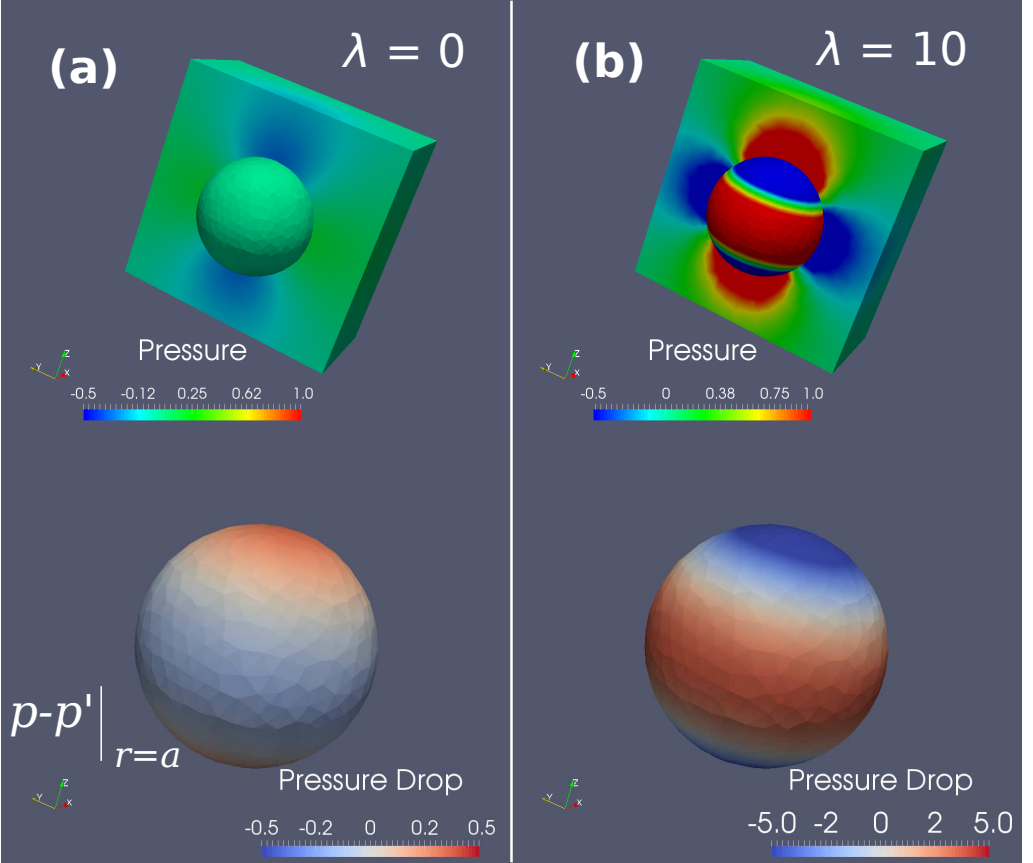


FIGURE 5. (a) Map of pressure  $p$  within and outside the sphere for  $\beta = 1$ ,  $\lambda = 0$ , and  $a = 1$ . The surface of the sphere in the bottom shows the pressure drop at the interface. Only half of the pressure field in the substrate is shown to enable visualization of the sphere. (b) Same as in panel (a) for  $\lambda = 10$ . The color map in all 4 visualizations are scaled according to the colorbar shown in the figure.

The pressure within and outside the sphere is also strongly modulated by the value of  $\lambda$ . The plots in Figure 5 outline the pressure fields within both domains and pressure difference at the interface. For all of these visualizations,  $\beta = 1$ . Two features of the solutions for pressure are evident from these visualizations. First, The magnitude of

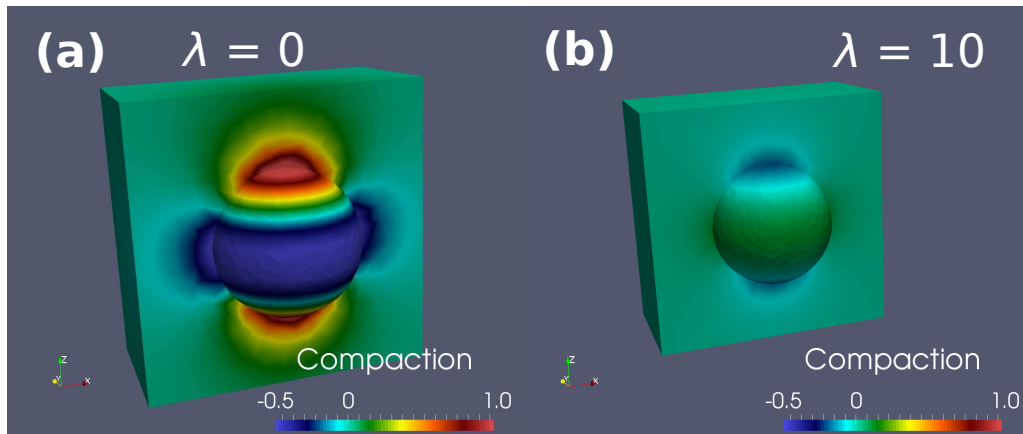


FIGURE 6. Map of compaction within and outside the sphere for (a)  $\lambda = 0$  and (b)  $\lambda = 10$ . For both visualizations,  $\beta = 1$ . As in Figure 5, only half of the substrate is shown. The color map within and outside the sphere are scaled according to the color bars shown in the panels.

pressure within the sphere increases with an increase in  $\lambda$ . Second, as a consequence, the difference in pressures at the poles and the equator undergo substantial changes. The bottom panel in both figures illustrate this change, as  $p - p'$  at  $r = a$  changes sign both at the pole and the equator, in response to an increase in  $\lambda$ . This observation is similar to the observations from the plot in Figure 7, described later.

Compaction,  $\mathcal{C} = \nabla \cdot \mathbf{u}$ , within and outside the sphere are closely related, as shown by the visualization in Figure 6. Similar to pressure, compaction within the sphere and the substrate also undergo a change in sign as the value of  $\lambda$  increases from 0 to 1. In addition, the magnitude of the compaction within both domains decrease with an increase in  $\lambda$ , as demonstrated by the intensity of colors in both panels.

The map of compaction within the sphere can also help in understanding the flow of melt within each domain, at least initially. Recall from equation (3.8),  $D\phi/Dt \approx \mathcal{C}$  for small values of  $\phi$ . Such a zeroth order approximation is only valid for a very short period of time after the onset of flow. This assumption becomes invalid as deformation progresses both within the sphere and the substrate. Keeping this limitation in mind, we notice that the polarity of fluid segregation reverses with a change in the viscosity ratio. For an inviscid sphere matrix, the interstitial fluid collects near the pole of the sphere ( $D\phi/Dt > 0$  at the pole), while the fluid drains away from the pole when  $\lambda = 10$  ( $D\phi/Dt < 0$  at the pole).

#### 4.2. The influence of bulk viscosity

The influence of  $\alpha = \beta\eta$ , the effective bulk viscosity, is unique to multiphase aggregates. As mentioned earlier, even if both the matrix and the interstitial fluid are incompressible, due to the presence of compaction, the two-phase aggregate has a nonzero effective bulk viscosity (McKenzie 1984; Ricard *et al.* 2001; Simpson *et al.* 2010a).

The normal component of traction at the interface between the sphere and the substrate shows a nonlinear variation with  $\lambda$  in Figure 7. The plot in this figure corresponds to the value of  $\mathbf{t} \cdot \hat{\mathbf{n}}$  evaluated at the north pole ( $x = 0, y = 0, z = a$ ) and at a point on the equator ( $x = a, y = 0, z = 0$ ). For a value of  $\lambda = 0$ , the inviscid matrix of the inner domain doesn't support stress, rendering the normal traction zero in both domains. For higher values of  $\lambda$ , the signs of the normal components are opposite at the north pole and at the equator, which are under compression and extension, respectively. As the viscosity

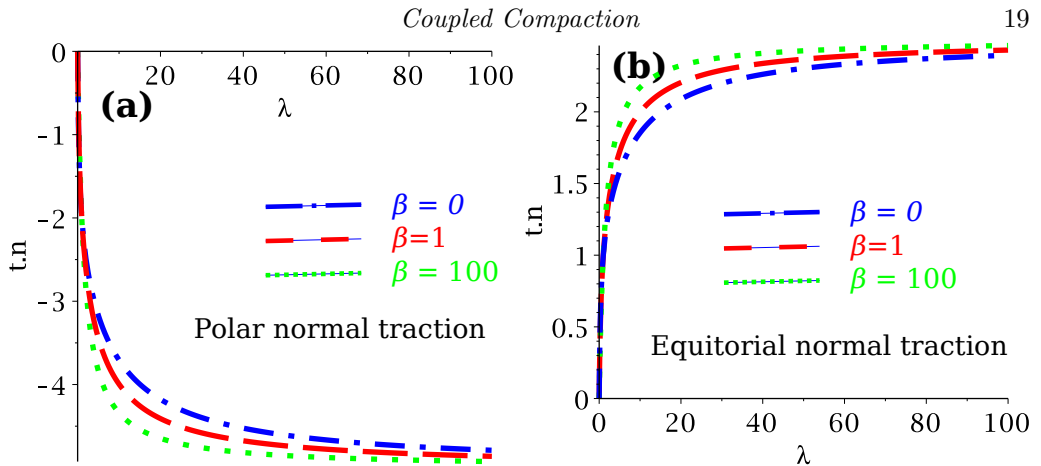


FIGURE 7. Plots of magnitude of (a) polar (evaluated at  $x = 0, y = 0, z = a$ ) and (b) equatorial (evaluated at  $x = a, y = 0, z = 0$ ) values of the normal traction as a function of the viscosity ratio,  $\lambda$ , for three different values of  $\beta$ , the ratio between bulk and shear viscosity of the matrix.

of the sphere increases, increasing the value of  $\lambda$ , the magnitude of both components of the normal traction increase, eventually saturating near a value of  $\lambda = 80$ . This observation implies that viscous coupling between the matrices within the sphere and the substrate (as our formulation considers the fluid phase within each aggregate bears no stress) should saturate at these values of  $\lambda$ . In understanding the viscous coupling between structures in the deep Earth, this limit can be important (Hier-Majumder & Revenaugh 2010; Hier-majumder & Tauzin 2017). The curves for three different values of  $\beta$  are shown in the plot. For higher values of  $\beta$ , the increase in the magnitude of normal traction are slightly higher. Compared with the influence of  $\lambda$ , however, the dependence of normal traction on  $\beta$  is weaker.

The plots in Figure 8 illustrate the variation in  $p - p'$  at  $r = a$  at the North pole and the equator. Two important features of these plots are the reversal in the sign of  $p - p'$  and the weak dependence on  $\beta$ . For a weak sphere matrix ( $0 < \lambda < 1$ ), the pressure drop displays a maximum and then changes sign as the value of  $\lambda$  increases above unity. When  $\lambda = 1$ , flow in both the sphere and the substrate are the same as the imposed far field flow. In the absence of the perturbation arising from the variations in matrix viscosity, the pressure within both domains are the same, rendering  $p = p'$  when  $\lambda = 1$ . Similar to normal traction, the curves display a weak dependence on  $\beta$  as the maximum shifts to a lower value and the position of the maximum shifts to a slightly higher value of  $\lambda$ , as  $\beta$  increases.

## 5. Discussion and Conclusions

The analytical solutions in this article demonstrate the importance of coupling of multiphase flow between two interacting domains. The analytical solutions presented in this work bear important implications for flow magnitude and phase segregation for natural flows. In a recent numerical investigation of coupled flow within the ULVZ and LLSVP system, Hier-Majumder & Drombosky (2016) posited that the lower viscosity ULVZ is strongly deformed by straining flow in the surrounding LLSVP. Due to the Stokes flow equation used within both domains, however, this work was unable to identify regions of compaction and phase segregation within the ULVZ. The results from the current work support their first conclusion, as the visualizations in Figure 4 demonstrate. Additionally,

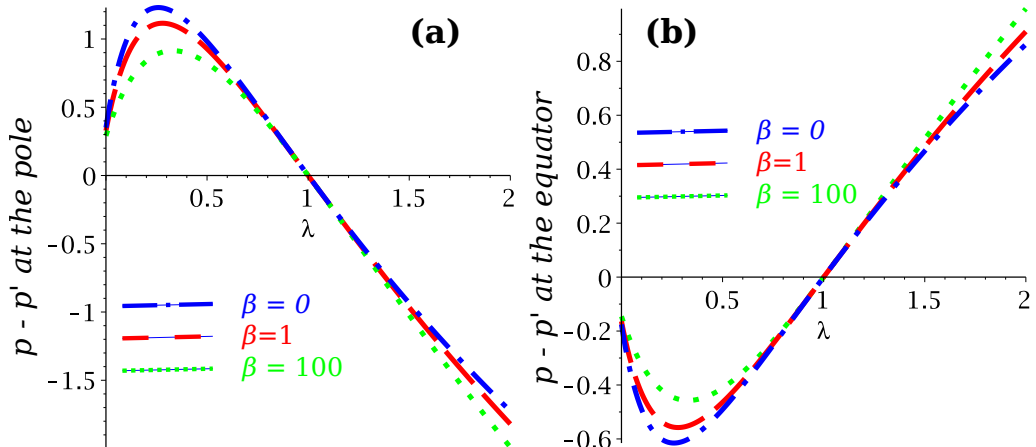


FIGURE 8. Plots of magnitude of polar and equatorial pressure difference between the internal and external fluid (a) at the pole and (b) at the equator as a function of  $\lambda$ , the ratio between matrix viscosities of the sphere and the substrate. As in Figure 7, the polar value of  $p - p'$  is evaluated at  $x = 0, y = 0, z = a$  and the equatorial value of  $p - p'$  is evaluated at  $x = a, y = 0, z = 0$ .

the map of compaction within the spherical domain, shown in Figure 6, is now able to provide a zeroth order approximation of the spatial distribution of compaction and decompaction within the sphere, a first step in understanding the internal structure of the ULVZs. Future work on solution building for a generalized far-field flow will be extremely beneficial for further understanding of such coupled flow. In another recent study of compaction in a one-dimensional melt column within the ULVZ, Hier-Majumder (2014) demonstrate the interstitial melt segregates near the top of the ULVZ during pulsed compaction. The results from this article show that melt segregation will occur near the compressive, polar region of a low viscosity ULVZ. To fully quantify the segregation of the interstitial fluid, however, it is important to study the coupled two-phase flow in three dimensions. In addition, the extent of fluid segregation will be strongly modulated by the ratio of the matrix shear viscosity of a ULVZ patch and the surrounding mantle.

The results presented in this article suffer from a few limitations resulting from the assumptions. The results focus primarily on the influence of the contrast in matrix shear viscosity within the two domains. In addition to the viscosity ratio,  $\lambda$ , the compaction length,  $\delta$  within the two domains should also play a significant role in coupling the flow. These solutions assume that the compaction length within domains is the same as the radius of the sphere. This assumption, however, can become invalid by a number of naturally occurring phenomena. In addition, mobility of the interstitial fluid can also vary between the two domains, a phenomenon not considered in this article, as we assume these values are same in both domains. Variations in fluid mobility across the interface will influence the solutions through the boundary conditions for continuity of flux. Such variations will provide additional perturbations to the flow, and the reversal of sign in the pressure and compaction at  $\lambda = 1$  may no longer be observed under such conditions. Finally, these analytical solutions are strictly valid for very small time scales following the onset of flow. To fully investigate the nature of the coupled nonlinear flow, future numerical simulations will be extremely helpful.

In conclusion, this article builds the solutions for coupled multiphase, multicomponent flow by decomposing the matrix velocity and reduced fluid pressure within each domain into two scalar functions  $\chi$  and  $\mathcal{C}$ , and a vector function  $\phi$ . We study the behavior of the solutions as a function of the ratio of matrix shear viscosities within and outside the

sphere. Our results indicate that velocity within the sphere is highest when this ratio is zero, and the magnitude of this velocity drops sharply as the ratio increases. We also notice that the magnitude of the polar and equatorial normal tractions at the surface of the sphere increase from zero to a finite value around  $\lambda = 80$ . This indicates that the effective rigidity of the spherical domain is achieved around this value of  $\lambda$ . Finally, we notice that the the sign of compaction and pressure at the interface between the sphere and the substrate undergo a change in sign at the poles and the equator, as the viscosity ratio,  $\lambda$  increases from 0 to 1.

## Acknowledgment

The work in this manuscript was supported by an NSF grant EAR 1215800. The author is extremely grateful for constructive comments by three anonymous reviewers and editor John Wettlaufer. Software associated with the analytical solution building and visualization is available for download at <https://doi.org/10.5281/zenodo.838655>.

## Appendix A. Governing equations

The complete set of governing equations within each domain consists of a mass and momentum conservation equation for each phase supplemented by a set of constitutive equations arising from the conservation of entropy and Onsager principle (Bercovici *et al.* 2001a; Rudge *et al.* 2011; Sramek *et al.* 2006). For the sake of brevity, the reader is referred to these references for a detailed derivation of the governing equations. Here we present a short derivation of the equations in terms of matrix velocity and reduced fluid pressure. The resultant equations are similar to those obtained by Rudge (2014).

In the absence of melting or freezing, the equation for conservation of mass of the matrix can be expressed as,

$$\frac{\partial \phi}{\partial t} = \nabla \cdot ((1 - \phi)\mathbf{u}), \quad (\text{A } 1)$$

where  $\mathbf{u}$  is the velocity and  $1 - \phi$  is the volume fraction of the matrix. This equation can be also rewritten as

$$\frac{D\phi}{Dt} = \frac{\partial \phi}{\partial t} + \mathbf{u} \cdot \nabla \phi = (1 - \phi)\nabla \cdot \mathbf{u}. \quad (\text{A } 2)$$

The material time derivative of the fluid volume fraction on the left hand side of equation (A 2) represents the rate of fluid loss or gain from a unit volume of the multiphase aggregate. The unit volumes within each domain are shown in the schematic diagram in Figure 1. Since the fluid volume fraction depends on time and space, this derivative is nonzero, rendering the matrix velocity divergent.

Since there are two phases, we need a second equation for conservation of mass of the interstitial fluid, given by

$$\nabla \cdot (\mathbf{u} - \phi \Delta \mathbf{u}) = 0, \quad (\text{A } 3)$$

where  $\Delta \mathbf{u}$  is the velocity of segregation between the fluid and the matrix.

In both domains, the matrix acts as the load bearing unit. As a result, the average normal traction across the sphere-substrate interface will be borne by the matrix on each domain. To evaluate this, we start with the definition of the stress tensor in the matrix,  $\mathbf{T}$ , using the constitutive relation,

$$\mathbf{T} = - \left[ \frac{2\eta}{3} \nabla \cdot \mathbf{u} + P_m \right] \mathbf{I} + \eta \boldsymbol{\varepsilon}(\mathbf{u}), \quad (\text{A } 4)$$

where  $P_m$  is the pressure within the matrix. In the microscopic scale, the representative elementary volume of the partially molten aggregate is occupied by two fluids of distinct physical properties, separated by a clear phase boundary. Under hydrostatic conditions, in the absence of surface tension, the pressure in both phases are equilibrated, *i.e.*  $P_m = P_f$ . Deformation of the viscous matrix, however, leads to a departure from this equilibrium state. Even if both fluid phases are incompressible with a constant density, the pressure difference between the two phases is balanced by the volumetric strain (compaction,  $\mathcal{C}$ ) in the matrix. This phenomenon leads to a nonzero bulk viscosity of the aggregate. Notice that this bulk viscosity term applies to both phases in the representative elementary volume, not just to one of the constituent phases.

The constitutive equation linking the pressure difference between the matrix and the fluid has been discussed in a number of previous works (Bercovici *et al.* 2001a; McKenzie 1984; Rudge *et al.* 2011; Simpson *et al.* 2010a). We refer the interested reader to these articles for more information on various notations and techniques used to derive this constitutive equation and Ricard *et al.* (2001, Section 2) for fluid segregation under different conditions of applied stress. Here, we use the constitutive equation proposed by Bercovici *et al.* (2001a) and modified by Hier-Majumder *et al.* (2006). In the absence of surface tension, the pressure difference between the matrix and the interstitial fluid is balanced by compaction Bercovici *et al.* (2001a)

$$P_m - P_f = -\frac{4\eta}{3\phi(1-\phi)} \frac{D\phi}{Dt} = -\frac{4\eta}{3\phi} \mathcal{C}. \quad (\text{A } 5)$$

Notice that the above definition of pressure difference between the two phases holds in the absence of mass exchange between the interstitial fluid and the matrix and zero surface tension (Takei & Hier-Majumder 2009).

The mass conservation equations are supplemented by two coupled partial differential equations (PDEs) for momentum conservation. First, the equation for momentum conservation in the matrix is given by,

$$\nabla \cdot \left[ \frac{4\eta}{3\phi} ((1-\phi) \nabla \cdot \mathbf{u}) \right] + \nabla \cdot \left[ \eta(1-\phi) \left( \boldsymbol{\varepsilon}(\mathbf{u}) - \frac{2}{3} (\nabla \cdot \mathbf{u}) \mathbf{I} \right) \right] - \frac{1}{\phi} \mathbf{C} \cdot \Delta \mathbf{u} = 0, \quad (\text{A } 6)$$

where  $\eta$  is the shear viscosity of the matrix,  $\mathbf{I}$  is the unit tensor,  $\mathbf{C}$  is the frictional resistance tensor,  $\Delta \mathbf{u}$  is the segregation velocity of the interstitial fluid, and the symmetric gradient operator  $\boldsymbol{\varepsilon}(\mathbf{u})$  is defined as

$$\boldsymbol{\varepsilon}(\mathbf{u}) = \nabla \mathbf{u} + (\nabla \mathbf{u})^T. \quad (\text{A } 7)$$

The first term in equation (A 6) arises from compaction, the second term from viscous deformation of the matrix, and the last term arises from friction between the two phases at the phase boundaries within each domain. This force of friction is experienced by both phases in equal and opposite amount (Bercovici *et al.* 2001a).

Assuming the viscosity of the interstitial fluid is substantially lower than the matrix, we neglect viscous stresses within the fluid. The momentum conservation equation for the fluid then becomes,

$$-\nabla P_f - \rho_f \mathbf{g} + \frac{1}{\phi} \mathbf{C} \cdot \Delta \mathbf{u} = 0 \quad (\text{A } 8)$$

where  $P_f$  is the pressure of the interstitial fluid,  $\rho_f$  is its density and  $\mathbf{g}$  is the gravity. Notice that equation (A 8) is a modified version of the Darcy flow equation.

We aim to reduce the system of governing equations into two PDEs in two unknown variables. To achieve this goal, we eliminate  $\Delta \mathbf{u}$  between equations (A 3), (A 6), and (A 8).

We also define the reduced pressure  $p$  as

$$p = P_f + \rho_f g z, \quad (\text{A } 9)$$

leading to the two PDEs in  $\mathbf{u}$  and  $p$ , within each domain  $\Omega_i (i = 1, 2)$ . Combining Equations (A 4), (A 5), and (A 9), in the absence of gravity, we arrive at the constitutive relation given in equation (2.6).

## REFERENCES

- ALISIC, LAURA, RUDGE, JOHN F, KATZ, RICHARD F, WELLS, GARTH N & RHEBERGEN, SANDER 2014 Journal of Geophysical Research : Solid Earth Compaction around a rigid , circular inclusion in partially molten rock pp. 5903–5920.
- ARFKEN, G.B. & WEBER, H. J. 1995 *Mathematical Methods for Physicists*, 4th edn. Academic Press.
- BARCILON, V. & LOVERA, O.M. 1989 Solitary waves in magma dynamics. *Journal of Fluid Mechanics* **204**, 121–133.
- BERCOVICI, D., RICARD, Y. & SCHUBERT, G. 2001a A two-phase model for compaction and damage; 1, General theory. *Journal of Geophysical Research, B, Solid Earth and Planets* **106** (5), 8887–8906.
- BERCOVICI, D., RICARD, Y. & SCHUBERT, G. 2001b A two-phase model for compaction and damage; 3, Applications to shear localization and plate boundary formation. *Journal of Geophysical Research, B, Solid Earth and Planets* **106** (5), 8925–8939.
- BOWER, DAN J., WICKS, JUNE K., GURNIS, MICHAEL & JACKSON, JENNIFER M. 2011 A geodynamic and mineral physics model of a solid-state ultralow-velocity zone. *Earth and Planetary Science Letters* **303** (3–4), 193 – 202.
- DREW, D.A. 1971 Averaged field equations for two-phase media. *Studies in Applied Mathematics* **50**, 133–166.
- DREW, D.A. 1983 Averaged field equations for two-phase flow. *Annu. Rev. Fluid Mech.* **15**, 261–291.
- DROMBOSKY, T. W. & HIER-MAJUMDER, S. 2015 Development of anisotropic texture in deforming partially molten aggregates i: Theory and fast multipole boundary elements method. *Journal of Geophysical Research, Solid Earth* **120**.
- GUNDE, AKSHAY C., BERA, BIJOYENDRA & MITRA, SUSHANTA K. 2010 Investigation of water and CO<sub>2</sub> (carbon dioxide) flooding using micro-CT (micro-computed tomography) images of Berea sandstone core using finite element simulations. *Energy* **35** (12), 5209–5216.
- HANDY, M. R., WISSING, S. B. & STREIT, L. E. 1999 Frictional-viscous flow in mylonite with varied biminerale composition and its effect on lithospheric strength. *Tectonophysics* **303** (1–4), 175–191.
- HAPPEL, J. & BRENNER, H. 1983 *Low Reynolds number hydrodynamics*. Kluwer.
- HIER-MAJUMDER, SASWATA 2008 Influence of contiguity on seismic velocities of partially molten aggregates. *Journal of Geophysical Research-Solid Earth* **113** (B12), B12205.
- HIER-MAJUMDER, S. 2011 Development of anisotropic mobility during two-phase flow. *Geophysical Journal International* **186**, 59–68.
- HIER-MAJUMDER, S 2014 Melt redistribution by pulsed compaction within ultralow velocity zones. *Phys. Earth and Planet. Int.* **229**, 134–143.
- HIER-MAJUMDER, SASWATA & ABBOTT, MATTHEW E. 2010 Influence of dihedral angle on the seismic velocities in partially molten rocks. *Earth and Planetary Science Letters* **299** (1–2), 23–32.
- HIER-MAJUMDER, S. & DROMBOSKY, T. W. 2015 Development of anisotropic texture in deforming partially molten aggregates ii: Implications for the lithosphere-asthenosphere boundary. *Journ. Geophys. Res.* **120**.
- HIER-MAJUMDER, SASWATA & DROMBOSKY, TYLER W. 2016 Coupled flow and anisotropy in the UltraLow Velocity Zones. *Earth and Planetary Science Letters* **450**, 274–282.
- HIER-MAJUMDER, SASWATA & REVENAUGH, JUSTIN 2010 Relationship between the viscosity and topography of the ultralow-velocity zone near the core-mantle boundary. *Earth and Planetary Science Letters* **299** (3–4), 382–386.

- HIER-MAJUMDER, SASWATA, RICARD, YANICK & BERCOVICI, DAVID 2006 Role of grain boundaries in magma migration and storage. *Earth and Planetary Science Letters* **248** (3-4), 735–749.
- HIER-MAJUMDER, SASWATA & TAUZIN, BENOIT 2017 Pervasive upper mantle melting beneath the western US. *Earth and Planetary Science Letters* **463**, 25–35.
- HOLYOKE, CALEB W. & TULLIS, JAN 2006 Mechanisms of weak phase interconnection and the effects of phase strength contrast on fabric development. *Journal of Structural Geology* **28** (4), 621–640.
- HOPPER, R.W. 1993a Coalescence of two viscous cylinders by capillarity: Part I, Theory. *Journal of the American Ceramics Society* **76**, 2947–2952.
- HOPPER, R.W. 1993b Coalescence of two viscous cylinders by capillarity: Part II, Shape evolution. *Journal of the American Ceramics Society* **76**, 2953–2960.
- KATZ, R F, KNEPLEY, M G, SMITH, B, SPIEGELMAN, M & COON, E T 2007 Numerical simulation of geodynamic processes with the Portable Extensible Toolkit for Scientific Computation. *Physics of The Earth and Planetary Interiors* **163**, 52–68.
- KIM, S. & KARILLA, S. J. 2005 *Microhydrodynamics: Principles and selected applications*, chap. 13. Dover.
- KING, D. S. H., HIER-MAJUMDER, S. & KOHLSTEDT, D. L. 2011 An experimental study of the effects of surface tension in homogenizing perturbations in melt fraction. *Earth and Planetary Science Letters* **307** (3-4), 735–749.
- KUIKEN, H.K. 1993 Viscous sintering: The surface-tension-driven flow of a liquid form under the influence of curvature gradient at its surface. *Journal of Fluid Mechanics* **214**, 503–515.
- LEAL, G. 1992 *Laminar Flow and Convective Transport Processes*. Butterworth-Heinemann.
- LI, X. & POZRIKIDIS, C. 1996 Shear flow over a liquid drop adhering to a solid surface. *Journal of Fluid Mechanics* **307**, 167–190.
- LI, X. & POZRIKIDIS, C. 1997 The effect of surfactants on drop deformation and on rheology of dilute emulsions in stokes flow. *Journal of Fluid Mechanics* **341**, 165–194.
- LI, XIAOFAN, ZHOU, HUA & POZRIKIDIS, C. 1995 A numerical study of the shearing motion of emulsions and foams. *Journal of Fluid Mechanics* **286**, 379–404.
- LOEWENBERG, M. & HINCH, E. J. 1996 Numerical simulation of a concentrated emulsion in shear flow. *Journal of Fluid Mechanics* **321** (-1), 395.
- MANGA, MICHAEL, CASTRO, JONATHAN, CASHMAN, KATHARINE V. & LOEWENBERG, MICHAEL 1998 Rheology of bubble-bearing magmas. *Journal of Volcanology and Geothermal Research* **87** (1-4), 15–28.
- MANGA, M. & LOEWENBERG, M. 2001 Viscosity of magmas containing highly deformable bubbles. *Journal of Volcanology and Geothermal Research* **105** (1-2), 19–24.
- MANGA, M. & STONE, H.A. 1995 Low reynolds number motion of bubbles, drops, and rigid spheres through fluid-fluid interfaces. *Journal of Fluid Mechanics* **287**, 279–298.
- MCKENZIE, D. 1984 The generation and compaction of partially molten rock. *Journal of Petrology* **25**, 713–765.
- MCMANARA, ALLEN K., GARNERO, EDWARD J. & ROST, SEBASTIAN 2010 Tracking deep mantle reservoirs with ultra-low velocity zones. *Earth and Planetary Science Letters* **299** (1-2), 1–9.
- POZRIKIDIS, C. 1990 The deformation of a liquid drop moving normal to a plane wall. *Journal of Fluid Mechanics* **215**, 331–363.
- POZRIKIDIS, C. 2001 Interfacial dynamics for stokes flow. *Journal of Computational Physics* **169**, 250–301.
- QI, CHAO, ZHAO, YONG HONG & KOHLSTEDT, DAVID L. 2013 An experimental study of pressure shadows in partially molten rocks. *Earth and Planetary Science Letters* **382**, 77–84.
- RHEBERGEN, SANDER, WELLS, GARTH N., KATZ, RICHARD F. & WATHEN, ANDREW J 2014 Analysis of block preconditioners for models of coupled magma/mantle dynamics. *SIAM J. Sci. Comput.* **36** (4), A1960–A1977.
- RHEBERGEN, SANDER, WELLS, GARTH N., WATHEN, ANDREW J. & KATZ, RICHARD F. 2015 Three-field block-preconditioners for models of coupled magma/mantle dynamics, arXiv: 1411.5235.
- RICARD, Y., BERCOVICI, D. & SCHUBERT, G. 2001 A two-phase model for compaction and



- damage; 2, Applications to compaction, deformation, and the role of interfacial surface tension. *Journal of Geophysical Research, B, Solid Earth and Planets* **106** (5), 8907–8924.
- ROST, S., GARNERO, E. J., WILLIAMS, Q. & MANGA, M. 2005 Seismological constraints on a possible plume root at the core-mantle boundary. *Nature* **435**, 666–669.
- ROST, S. & REVENAUGH, J. 2003 Small scale ultralow-velocity zone structure imaged by *ScP*. *Journal of Geophysical Research* **108** (B12056).
- RUDGE, JOHN F. 2014 Analytical solutions of compacting flow past a sphere. *Journal of Fluid Mechanics* **746**, 466–497.
- RUDGE, JOHN F., BERCOVICI, DAVID & SPIEGELMAN, MARC 2011 Disequilibrium melting of a two phase multicomponent mantle. *Geophysical Journal International* pp. 699–718.
- RUST, A.C. & MANGA, MICHAEL 2002 Effects of bubble deformation on the viscosity of dilute suspensions. *Journal of Non-Newtonian Fluid Mechanics* **104** (1), 53–63.
- SIMPSON, G., SPIEGELMAN, M. & WEINSTEIN, M. I. 2010*a* A multiscale model of partial melts: 1. effective equations. *J. Geophys. Res.* **115** (B04410), doi:10.1029/2009JB006375.
- SIMPSON, G., SPIEGELMAN, M. & WEINSTEIN, M. I. 2010*b* A multiscale model of partial melts: 2. numerical results. *J. Geophys. Res.* **115** (B04411), doi:10.1029/2009JB006376.
- SPIEGELMAN, M. 1993*a* Flow in deformable porous media, part 1, Simple analysis. *Journal of Fluid Mechanics* **247**, 17–38.
- SPIEGELMAN, M. 1993*b* Flow in deformable porous media, part 2, Numerical analysis—the relationship between shock waves and solitary waves. *Journal of Fluid Mechanics* **247**, 39–63.
- SRAMEK, RICARD, Y. & BERCOVICI, D. 2006 Simultaneous melting and compaction in deformable two-phase media. *Geophysical Journal International* **168**, 964–982.
- TAKEI, YASUKO & HIER-MAJUMDER, SASWATA 2009 A generalized formulation of interfacial tension driven fluid migration with dissolution/precipitation. *Earth and Planetary Science Letters* **288** (1–2), 138–148.
- TAYLOR, G. 1932 The viscosity of a fluid containing small drops of another fluid. *Proc. Roy. Soc. (London)* **138** (834), 41–48.
- WILLIAMS, Q. & GARNERO, E.J. 1996 Seismic evidence for partial melt at the base of Earth’s mantle. *Science* **273**, 1528–1530.
- WIMERT, J. T. & HIER-MAJUMDER, S 2012 A three-dimensional microgeodynamic model of melt geometry in the earth’s deep interior. *Journal of Geophysical Research-Solid Earth* **117** (B04), B04203.